Numerical and experimental investigation of impacts of nonlinear scattering encapsulated microbubbles on Nakagami distribution

Diya Wang
University of Montreal Hospital Research Center, Montreal, QC H2X 0A9, Canada
Department of Biomedical Engineering, School of Life Science and Technology, Xi'an Jiaotong University, Xi'an 71049, P. R. China

Yuchao Sang, Xinyu Zhang, Hong Hu, Shukuan Lu, and Yu Zhang
Department of Biomedical Engineering, School of Life Science and Technology, Xi'an Jiaotong University, Xi'an 71049, P. R. China

Chaoying Fu[a]
Center Lab of Longhua Branch and Department of Infectious disease, Shenzhen People's Hospital 2nd Clinical Medical College of Jinan University, Shenzhen 518120, China
Institut National de la Recherche Scientifique (INRS) EMT Center, Varennes, QC J3X 1S2, Canada

Guy Cloutier[a]
University of Montreal Hospital Research Center, Montreal, QC H2X 0A9, Canada

Mingxi Wan[a]
Department of Biomedical Engineering, School of Life Science and Technology, Xi'an Jiaotong University, Xi'an 71049, P. R. China

Purpose: The Nakagami statistical model and Nakagami shape parameter m have been widely used in linear tissue characterization and preliminarily characterized the envelope distributions of nonlinear encapsulated microbubbles (EMBs). However, the Nakagami distribution of nonlinear scattering EMBs lacked a systematical investigation. Thus, this study aimed to investigate the Nakagami distribution of EMBs and illustrate the impact of EMBs' nonlinearity on the Nakagami model.

Method: A group of simulated EMB phantoms and *in vitro* EMB dilutions with an increasing concentration distribution under various EMB nonlinearities, as regulated by acoustic parameters, were characterized by using the window-modulated compounding Greenwood–Durand estimator.

Results: Raw envelope histograms of simulated and *in vitro* EMBs were well matched with the Nakagami distribution with a high correlation coefficient of 0.965 ± 0.021 ($P < 0.005$). The mean values and gradients of m parameters of simulated and *in vitro* EMBs were smaller than those of linear scatterers due to the stronger nonlinearity. These m values exhibited a quasi-linear improvement with the increase in second harmonic nonlinear-to-linear component ratio regulated by pulse lengths and excitation frequencies at low- and high-concentration conditions.

Conclusions: The Nakagami distribution was suitable for the EMBs characterization but the corresponding m parameter was affected by the EMBs' nonlinearity. These validations provided support and nonlinear impact assessment for the EMBs' characterization using the Nakagami statistical model in the future. © *2019 American Association of Physicists in Medicine* [https://doi.org/10.1002/mp.13833]

Key words: encapsulated microbubble, Greenwood–Durand estimator, Nakagami parameter, nonlinearity, window-modulated

1. INTRODUCTION

As an important clinical diagnosis tool, ultrasound B-mode imaging is coded by a power distribution of backscattered echoes and provides a qualitative description of the tissue morphology.[1] However, B-mode imaging impairs and even loses the inherent backscattered distribution related to tissue scatterers because their power distributions are affected by scanner parameters and sonographers.[2,3] Some useful quantitative ultrasound techniques, including probabilistic and statistical analyses, have been developed to supplement B-mode imaging for tissue characterization.[3,4] Considering the randomness of the ultrasonic backscattered signals, several statistical distributions with independent of scanner parameters

and sonographers were explored to model the probability density function (PDF, first-order statistics) of the backscattered echoes for tissue characterization.[5–9]

When a resolution cell of ultrasound transducer contains a number of randomly located scatterers, the PDF of the backscattered echo envelope is Rayleigh distributed.[5–9] Global statistics of the backscattered signals in a homogeneous medium can then be considered as the Rayleigh distribution.[10] However, the local scatterers in most biological tissues have various possibilities of arrangements and sizes, which can be modeled as a pre-Rayleigh distribution in heterogeneous media[11] and post-Rayleigh distribution in periodic texture.[4,12] Thus, homodyned K,[7] Nakagami,[13] and other distribution models have been used to approximate the PDF

in these heterogeneous and periodic textures, which can cover the pre- and post-Rayleigh distributions of tissue backscattered signals. Destrempes and Cloutier[14,15] and Oelze and Mamou[16] successively reviewed these envelope statistical models for quantitative ultrasound imaging in tissue characterization. In contrast, the homodyned K model has good generality and consistency, but its application is limited by a high algorithmic complexity.[14,15] As an approximation of the homodyned K distribution,[14,15] Nakagami distribution modeling can characterize a wide-range of scattering conditions from pre-Rayleigh to post-Rayleigh[3] with a good efficiency.[15,16] The Nakagami distribution was originally used to statistically evaluate radar signals and was first used to analyze ultrasonic backscattered echoes from tissues by Shankar et al.[12] Considering that the Nakagami shape parameter m is dependent on the shape, size, density, and other inherent properties of the scatterers,[17] m estimation has been used to classify the scattering properties of myocardium,[18] breast tumors,[19,20] liver fibrosis,[21] kidney disease,[22] protein coagulation,[23,24] and red blood cell aggregation.[25]

Although minor nonlinear propagation exists in tissues using regulated acoustic output standards for medical applications, tissue scatterers are always taken as linear scatterers (LSs) in statistical distributions of B-mode images. Compared with LSs, encapsulated microbubbles (EMBs) present stronger nonlinear harmonic scattering under clinical insonation conditions.[26] Phospholipid EMBs are widely used in dynamic contrast-enhanced ultrasound to augment the intravascular backscattered echo magnitude because of their unique scattering property.[27] In this context, EMBs have the possible opportunity to be characterized by envelope statistical distributions, particularly the m parameter of Nakagami model. The estimated m value under controllable injection concentration might provide a signature of physical parameters (e.g., shape, size, structure, and material) and acoustic properties (e.g., acoustic impedance and scattering cross-section area). A few studies used the m parameter to characterize nonlinear scattering by EMBs. Using parameters estimated from time-m dynamic curves, Gu et al.[28] and Tsui et al.[29] predicted the EMB-enhanced vascular flow. Kolar et al.[30] and Hu et al.[31] provided feasibility results on the concentrations of EMBs and cavitation bubbles, respectively. Zhang et al.[23,24] and Han et al.[17] classified the erosion and liquidation induced by cavitation bubbles during ultrasonic therapy.

However, the Nakagami distribution of EMBs requires further investigation under different experimental conditions, and a systematic analysis of the m parameter is also lacking. The nonlinear scattering properties of EMBs are quite different from scattering of LSs. Compared with tissues made of LSs, the nonlinearity of EMBs is more sensitive to transmission parameters of ultrasound scanners, including pressure, frequency, and duty cycles, etc. Currently, the impact of the nonlinearity of EMBs on Nakagami model and m parameter is unknown. Therefore, this study aimed to investigate the Nakagami distribution of B-mode images containing EMBs via simulations and *in vitro* experiments.

2. METHODS AND EXPERIMENTS

2.A. Window-modulated compounding Greenwood–Durand Nakagami parameter estimator

To ensure strong robustness of m estimation of EMB B-mode echo envelopes, we applied the window-modulated compounding strategy proposed by Tsui et al.[1] into the Greenwood–Durand (GD) m estimator,[32] as described in the following equation:

$$\overline{m_{GD}} = \frac{1}{M} \sum_{w=\lambda}^{w=M\lambda} \langle m_{GD} \rangle$$

$$= \frac{1}{M} \sum_{w=\lambda}^{w=M\lambda} \left\langle \left\{ \begin{array}{ll} \frac{(0.50008+0.16488\Delta-0.05442\Delta^2)}{\Delta} & 0<\Delta\leq0.5772 \\ \frac{8.89892+9.05995\Delta+0.97754\Delta^2}{\Delta\left(17.79728+11.96847\Delta+\Delta^2\right)} & 0.5572<\Delta<17 \end{array} \right\} \right\rangle$$

(1)

where λ and w are the triple wavelength and sample size, respectively; M is the modulation parameter, which was given a value of three in this study. m_{GD} is an approximate value of the Nakagami shape parameter within a fixed sample size obtained by the GD estimator. Δ is the following difference between the logarithm function $ln(m)$ and digamma equation $\psi(m)$.[18]

$$\Delta \approx ln(m) - \psi(m) = ln(m) - \Gamma'(m)/\Gamma(m)$$

(2)

where $\Gamma(m)$ is the Gamma function of m and Eq. (3) is then numerically expressed as follows[33]:

$$\Delta = ln\left[\left(\frac{1}{N} \sum_{i=1}^{N} R_i^2 \right) \Big/ \left(\prod_{i=1}^{N} R_i^2 \right)^{1/N} \right]$$

(3)

where R is the envelope signal of B-mode EMB echoes.

The GD estimator is a common maximum likelihood estimation method to estimate the m parameter[34] and is briefly introduced here; it is based on the following log-likelihood function of the joint PDF(R) of N samples ($R_i, i = 1, 2, \ldots, N$)[32]:

$$ln[\text{PDF}(R)] = ln\left[\prod_{i=1}^{N} \frac{2}{\Gamma(m)} k^m R_i^{2m-1} e^{-kR_i^2} \right]$$

(4)

where $k = m/\Omega$ is the ratio of m and Ω; and Ω is the scale parameter of the Nakagami statistical model. Here, PDF(R) is the joint Nakagami distribution function of the backscattered echo envelope R of N samples within a fixed resolution cell. The derivative of Eq. (4) was set to zero and Eqs. (2) and (3) were derived to obtain the maximum log-likelihood estimation. According to the first- and second-order approximations in Eq. (3), Greenwood and Durand then derived Eq. (1) as an approximate expression of Eq. (3).[32] The piecewise polynomial fitting in Eq. (1) showed that the GD method is stable for low-order approximation and accurate for high-order approximation, which could avoid the closed-form expression for local m estimation.[33]

2.B. Simulations

To illustrate the impact of nonlinear scattering produced by EMBs on the Nakagami distribution, EMB echoes had to be controlled by considering various transmission parameters of ultrasound scanners. Considering that the simulation can precisely mimic the concentration and distribution of EMBs, this study was first validated via simulations. EMB phantoms with an increasing concentration of contrast bubbles were produced by a convolution model coupling with the EMB scattering function in the Field II open-source software, as described in the following two steps:

First step: The total size of the EMB phantoms was 6×6 mm. By considering EMB concentrations in microvessels,[35–37] the simulated phantoms were set with an increasing concentration of EMBs ranging from 0.5 to 24 bubbles/mm^2. The average initial radius of EMBs was 1 μm.[38] A 64-element array transducer was defined by using the "xdc_linear_array" function in the Field II program (single element width = 0.2798 mm, height = 4 mm, and kerf = 0.025 mm). The number of subdivisions in the axial and lateral directions of elements was 5 and 2, respectively. The imaging parameters were then initialized. The transducer was excited by a default excitation pulse (frequency = 3 MHz, pulse length = 2 cycles, and negative peak pressure = 100 kPa). To avoid additional influences induced by a nonuniform acoustic field, double focus points of 11 and 15 mm were used and the EMB phantoms were then positioned at this focal region with a uniform acoustic field. The imaging depth range of phantoms was 10–16 mm. A Hanning window apodization was used and radiofrequency (RF) data were sampled at 50 MHz.

Second step: Backscattered EMB echoes were produced by using a convolution model[39] and embedded into the simulated EMB phantoms. The convolution model is briefly presented here; more details can be found in Ref. [[39]]. In this model, the RF data $\mathbb{R}(\vec{z}, t)$ from EMBs were produced by the convolution operator between the reflectivity function $f_c(\vec{z}, t)$ (linear component) and the point-spread-function $H_c(\vec{z}, t)$ of EMBs (nonlinear component), as in the following equation[39]:

$$\mathbb{R}(\vec{z}, t) = H_c(\vec{z}, t) * f_c(\vec{z}, t) + \eta(t) \tag{5}$$

where $\eta(.)$ is simulated background noise inherent to the acquisition process. $\vec{z}$ and t are the EMB location and the corresponding scattering time, respectively.[39] Here, $H_c(\vec{z}, t)$ was predicted by the following modified Herring vibration and scattering equations of EMBs.[40]

$$\rho \left[r(t)\ddot{r}(t) + \frac{3}{2}\dot{r}(t)^2 \right] = \left[P_0 + \frac{2\sigma}{r_0} + \frac{2\chi}{r_0} \right] \left[1 - \frac{3\gamma}{c}\dot{r}(t) \right] \left[\frac{r_0}{r(t)} \right]^{3\gamma}$$
$$- \frac{4\mu\dot{r}(t)}{r(t)} - \frac{2\sigma}{r(t)} \left[1 - \frac{1}{c}\dot{r}(t) \right]$$
$$- \frac{2\chi}{r(t)} \left[1 - \frac{3}{c}\dot{r}(t) \right] \left[\frac{r_0}{r(t)} \right]^2$$
$$- 12\mu_{sh}\varepsilon \frac{\dot{r}(t)}{r(t)[r(t) - \varepsilon]} - [P_0 + P_{driv}(t)] \tag{6}$$

$$H_c(\vec{z}, t) = \frac{f}{BF} \left\{ \rho \left[r(t)^2 \ddot{r}(t) + r(t)\dot{r}(t) \right] / |\vec{z}| \right\} \tag{7}$$

where r_0 and $r(t)$ are the initial radius and instantaneous radial vibration curves of EMBs, respectively; and $\dot{r}(t)$ and $\ddot{r}(t)$ are the first- and second-order derivatives of radial curves, respectively. Moreover, ρ, μ, and c are the density, viscosity, and acoustic speed in liquid media, respectively. σ, χ, μ_{sh}, and ε are the interfacial tension coefficient, elasticity modulus, viscosity, and thickness of the lipid shell, respectively. γ is the polytropic gas exponent. P_0 and $P_{driv}(t)$ are the hydrostatic pressure and the acoustic pressure of the excitation pulse, respectively. These parameters were defined in previous studies.[38,41] $\frac{f}{BF}$ is a band-pass filter determined by the actual bandwidth of the transducer. According to the spatial distribution of EMBs in the first step, backscattered echoes produced by EMBs were finally embedded in the simulated phantoms to consider conditions with an increasing concentration of EMBs. Besides, as a control group, simulated phantoms with LSs were also produced at the same concentrations to compare results with simulated EMB phantoms.

2.C. *In vitro* experiments

Although the concentration and distribution of EMBs are extremely difficult to be precisely controlled under *in vitro* and *in vivo* conditions, the feasibility of the simulated results was investigated via *in vitro* experiments. EMB solutions (average radius = 1.25 μm[38]; SonoVue, Bracco, Milan, Italy) at an increasing concentration were produced using degassed normal saline (0.9%, sodium chloride). The increasing concentration of EMBs ranged from about 4 to 64 bubbles/mm^3. RF data of EMB echoes (n = 3 per concentration) at the above described concentrations were recorded by using a Sonix-touch scanner (−6 dB bandwidth: 2–10 MHz; Ultrasonix Medical Corporation, Richmond, BC, Canada) equipped with a 128-element array transducer at a sampling frequency of 40 MHz. The transducer was excited by a default excitation pulse (frequency = 3.3 MHz, pulse length = 1 cycle, negative peak pressure = 200 kPa, and focal depth = 30 mm). To ensure a similar concentration and uniform distribution of EMBs among successive frames at the same concentration, the frame rate was set at 40 Hz and a magnetic stirrer (#85-2, Pudong Optical-physics Instrument Inc., Shanghai, China) was used to mix these dilutions during experiments at a rate of 300–500 rpm. To avoid influences of a nonuniform acoustic field, a calibrated hydrophone (#HGL-0085, ONDA, Sunnyvale, CA, USA) was used before experiments to select samples of 150×60 data points in postfocal regions, where the acoustic field was relatively uniform. Besides, for the control group of LSs, graphite powders (average radius = 1.3 μm; Aladdin, Shanghai, China) were diluted in saline at the same concentrations to compare results of *in vitro* EMB dilutions.

2.D. Simulated and *in vitro* acoustic parameters

The EMBs' nonlinearity could be regulated by controlling the acoustic parameters of the excitation pulse. In simulations, the excitation frequency was set to 2, 3, 5, and 7 MHz; the pulse length was chosen to be 1, 2, 3, and 4 cycles; and the negative peak pressure was selected at 50, 100, and 200 kPa. In *in vitro* experiments, the frequency was set to 2, 3.3, and 5 MHz; the pulse length was selected as 1, 2, 3, and 4 cycles; and the negative peak pressure for these conditions corresponded to values of about 100, 150, and 200 kPa, which was measured using the hydrophone. Other parameters were kept at the default setting when a certain parameter was changed.

2.E. Data processing and analysis

All simulated and *in vitro* B-mode envelopes were detected after Hilbert transform. Using the window-modulated compounding average effect with a small estimation error,[1] the modulation sliding-window traversed the entire region of the above envelopes and the local value $\overline{m_{GD}}$ was then estimated by using the proposed compounding GD estimator. A group of *m* parametric maps with increasing concentration of EMBs was formed after color coding. These *m* parametric maps were adjusted to the same dynamic range for proper comparison.

The histograms of RF envelope data of simulated EMB phantoms and *in vitro* EMB dilutions were calculated and the corresponding Nakagami-fitted PDFs were computed. The correlation coefficients between histograms and Nakagami-fitted PDFs were calculated and further evaluated by using paired t-tests and Kolmogorov–Smirnov tests.

The relationship between the *m* parameter and the EMB concentrations was built. The simulated phantoms and *in vitro* EMB dilutions were divided into the low- and high-concentration groups according to the concentration–*m* parameter curve to investigate the impact of EMBs' nonlinearity. We took concentrations of 1 and 16 particles/mm^2 in simulations and 8 and 32 particles/mm^3 in experiments to separate the low- and high-concentration conditions, respectively. The nonlinear scattering of simulated and *in vitro* EMBs was quantified by using the following second harmonic nonlinear-to-linear component ratio (NLCR). The NLCRs of EMBs under various acoustic parameters mentioned above were calculated

$$NLCR = P_{2f_0}/P_{f_0} \tag{8}$$

where P_{f_0} and P_{2f_0} are the areas of fundamental and second harmonic components, respectively, within a bandwidth of 20% in the power spectrum density curves of EMB echoes. The influence of the EMBs' nonlinearity on the Nakagami distribution was evaluated by using the mean and gradient values of *m* parameters under various NLCR values induced by adjustable pulse parameters. The gradient values were the corresponding change rates of *m* parameters with the increasing concentration. The slopes of mean and gradient values of

m parameters with acoustic parameters and NLCRs were further analyzed in this study.

Besides, as the ground truth, another group of simulated phantoms with a known *m* parameter ranging from 0.1 to 2.0 and a fixed scaling factor Ω was built through the Nakagami distribution function in MATLAB (Mathworks Inc., Natick, MA, USA). The window size was set from 50 to 1000 at two fixed *m* parameters of 0.5 and 1.5 to analyze the influence of the window size on *m* estimations. Thus, the efficiency and accuracy of the *m* estimation were evaluated by using the operation time and the root-mean-square error (RMSE) between the estimated value and simulated ground truth, respectively. The performance of the GD estimator was further compared with other *m* estimation methods, including the inverse normalized variance,[12] Lorenz,[13] Tolparev-Polyakov,[42] and Bowman[18] estimators. The mean and standard deviation of the above evaluations were calculated. All data analyses were conducted using MATLAB.

3. RESULTS

3.A. Nakagami distribution of nonlinear scattering produced by EMBs

Figure 1 shows the simulated and *in vitro* B-mode images of EMBs and LSs at increasing concentrations. Figure 2 displays the corresponding simulated and *in vitro* Nakagami *m* parametric maps. The B-mode images and *m* parametric maps of EMBs and LSs brightened with the increase in concentrations. However, the B-mode envelopes produced by EMBs had a larger dynamic range than those of LSs due to the strong nonlinear acoustic response. Figures 3(a) and 3(c) display the corresponding histograms and Nakagami-fitted PDFs of simulated and *in vitro* EMBs at increasing concentrations for the small second harmonic NLCR at 3 and 3.3 MHz conditions, respectively. Figures 3(b) and 3(d) show histograms and Nakagami-fitted PDFs for a large second harmonic NLCR at 2 MHz condition, respectively. These Nakagami-fitted PDFs matched the corresponding histogram distributions, of which the averaged correlation coefficient was 0.965 ± 0.021 ($P < 0.005$ in *t*-test and $P < 0.005$ in Kolmogorov–Smirnov test as given in Table I). The distributions of echoes from simulated and *in vitro* EMBs at various nonlinearity conditions were hence adequately modeled by Nakagami distributions, which were slightly different from the Nakagami distributions of simulated and *in vitro* LSs[3]. These results add to the lack of investigation of Nakagami distributions of nonlinear EMB echoes in previous studies.[4,30,31]

3.B. Impact of EMBs' nonlinearity on the Nakagami *m* parameter

Figures 4(a) and 4(c) shows simulated and *in vitro m* parameter curves of EMBs and LSs at increasing concentrations. At the same acoustic parameters used in Fig. 1, the Nakagami *m* parameters of EMBs were proportional to the
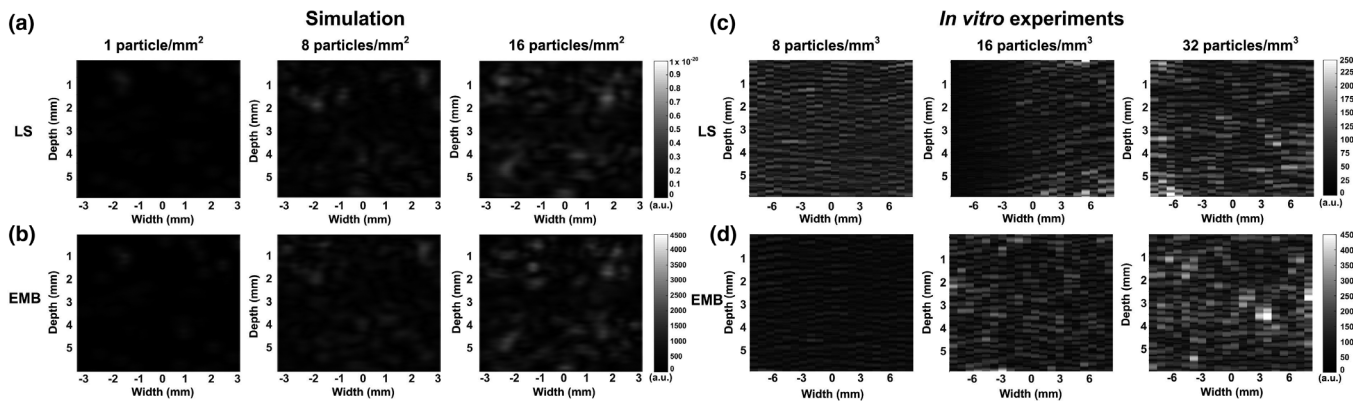
FIG. 1. Typical B-mode images of (a) simulated linear scatterers, (b) simulated nonlinear encapsulated microbubbles (EMBs), (c) *in vitro* LSs, and (d) *in vitro* EMBs at increasing concentrations. Simulated images are under a pulse length of 2 cycles, a negative peak pressure of 100 kPa, and a frequency of 3 MHz. *In vitro* images are under a pulse length of 1 cycle, a negative peak pressure of 200 kPa, and a frequency of 3.3 MHz. [Color figure can be viewed at wileyonlinelibrary.com]
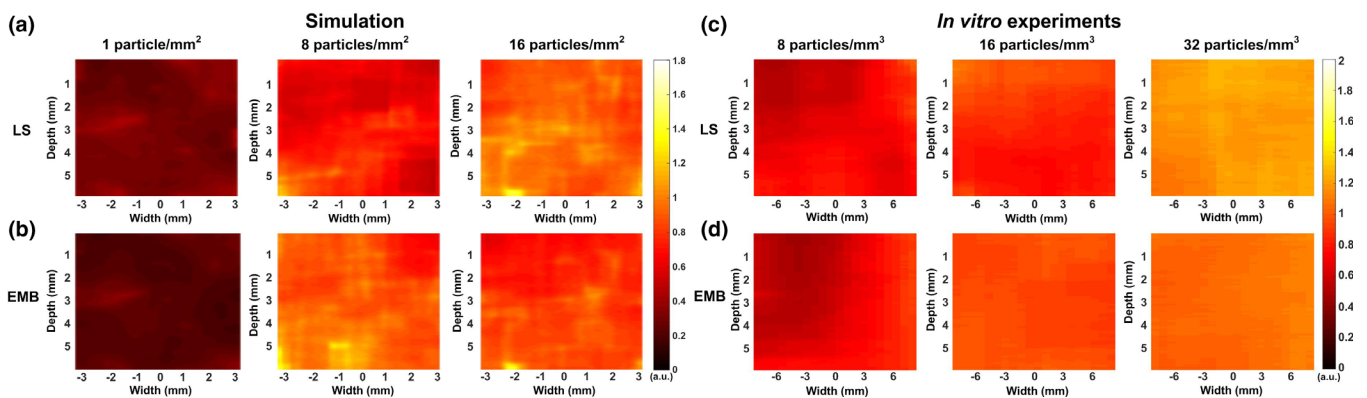

FIG. 2. The corresponding Nakagami m parametric maps of (a) simulated linear scatterers (LSs), (b) simulated encapsulated microbubbles (EMBs), (c) *in vitro* LSs, and (d) *in vitro* EMBs in Fig. 1 calculated by using the window-modulated compounding Greenwood–Durand (GD) estimator. [Color figure can be viewed at wileyonlinelibrary.com]

corresponding concentration distribution, which was similar to the concentration–m curve of LSs in previous studies.[3] Moreover, these concentration–m curves exhibited a piecewise quasi-linearly increasing tendency at the low- and high-concentration conditions. Inflection points in simulations and experiments were at 8 particles/mm^2 and 16 particles/mm^3, respectively. These concentration–m curves were not only consistent with previous concentration validations of EMBs[4,30,31] but also supplemented previous characterizations of EMBs[43] and LSs.[3] Thus, the Nakagami statistical model has the potential to characterize the relative concentration distribution of EMBs within a local resolution cell, although the EMBs present strong nonlinear acoustic behavior under acoustic insonation.[26]

The normalized power spectral densities in Figs. 4(b) and 4(d) show that the simulated and *in vitro* LS echo energy is concentrated at the fundamental frequency without harmonic components, but the simulated and *in vitro* EMBs had a strong second harmonic component in addition to the fundamental frequency. As shown in Fig. 5, the average NLCRs of LSs and EMBs were 0% and 7.8 ± 0.01% in simulations and 11.6 ± 0.6% and 15.3 ± 1.9% in experiments, respectively. Under these

NLCRs at the same acoustic parameters, the mean values and gradients of m parameters of EMBs and LSs were analyzed and compared for the low- and high-concentration segments in Fig. 5. Except for the gradient at the high concentration, the mean and change rate of m parameters of simulated and *in vitro* EMBs were smaller than those of LSs at the same particle distributions due to the nonlinear scattering of EMBs at large NLCRs. The m means of simulated EMBs were $7.6 ± 0.6 × 10^{-2}$ ($P = 0.002$) and $14.9 ± 2.3 × 10^{-2}$ ($P = 0.008$) smaller than those of LSs at the low- and high-concentration segments in Fig. 5(a), respectively. The corresponding simulated gradients were $2.8 ± 0.3 × 10^{-2}$ ($P = 0.004$) and $-0.3 ± 0.03 × 10^{-2}$ ($P = 0.04$) smaller than those of LSs in Fig. 5(b), respectively. These results indicate that the EMBs' nonlinearity influenced the echo envelopes and resulted in a left shift of Nakagami distributions compared with LSs.

3.C. EMBs' Nakagami parameter under various acoustic parameters

Figure 6 shows the impact of simulated EMBs' nonlinearity controlled by the pulse length, negative peak pressure, and
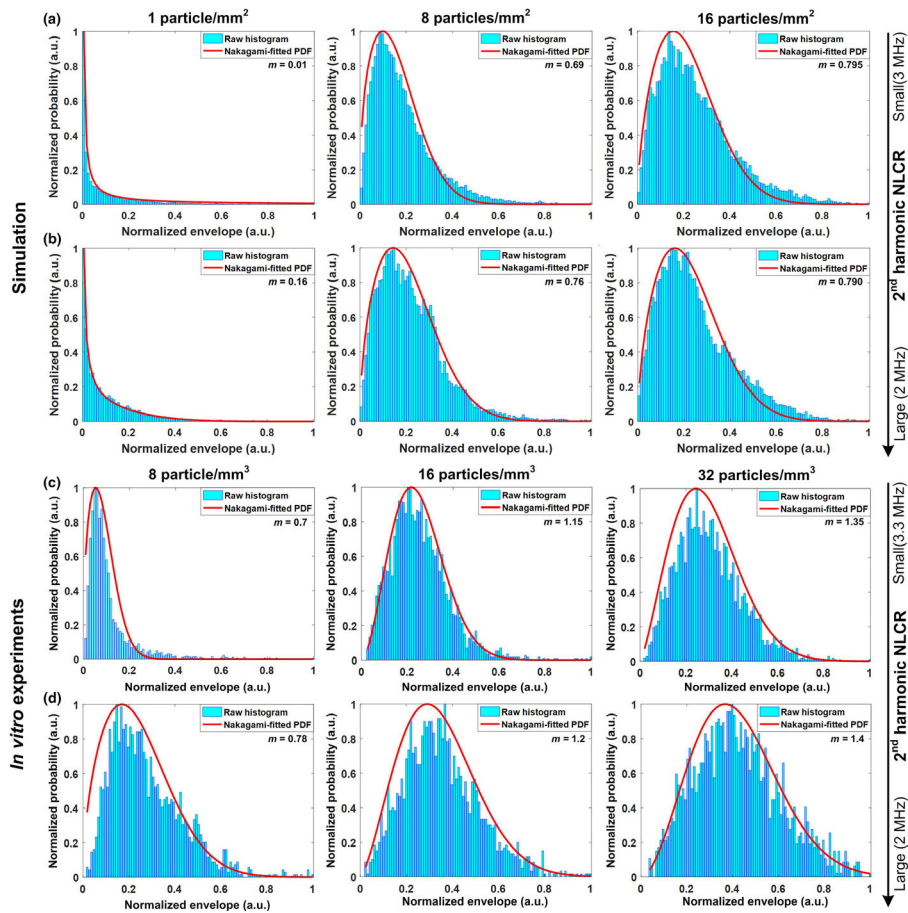
FIG. 3. Histograms and Nakagami-fitted probability density functions (PDF) of B-mode images corresponding to simulated encapsulated microbubbles (EMBs) at frequencies of (a) 3 MHz and (b) 2 MHz, respectively; and histograms and Nakagami-fitted PDFs of *in vitro* EMBs at work frequency of (c) 3.3 MHz and (d) 2 MHz, respectively. [Color figure can be viewed at wileyonlinelibrary.com]

TABLE I. Correlation coefficients, t-tests, and Kolmogorov–Smirnov tests in Fig. 3.

Acoustic parameters	Concentration	Correlation coefficient R^2	P value in t-test	P value in Kolmogorov–Smirnov test
Simulation				
2 MHz	1	0.995	2.2×10^{-14}	3.7×10^{-3}
100 kPa	8	0.952	4.8×10^{-4}	2.6×10^{-9}
2 cycles	16	0.953	2.2×10^{-7}	1.7×10^{-8}
3 MHz	1	0.998	4.0×10^{-5}	1.2×10^{-49}
100 kPa	8	0.951	2.9×10^{-3}	1.7×10^{-6}
2 cycles	16	0.935	6.6×10^{-4}	2.0×10^{-9}
In vitro				
2 MHz	8	0.941	1.1×10^{-6}	2.6×10^{-9}
200 kPa	16	0.969	3.6×10^{-13}	1.4×10^{-9}
1 cycle	32	0.957	4.5×10^{-6}	1.8×10^{-4}
3.3 MHz	8	0.958	4.0×10^{-3}	3.9×10^{-27}
200 kPa	16	0.981	1.7×10^{-13}	5.4×10^{-15}
1 cycle	32	0.989	7.1×10^{-4}	9.0×10^{-21}

Units in simulation are particles/mm².
in vitro experiments are particles/mm³.

frequency on mean values and gradients of Nakagami m parameters. With the increase in second harmonic NLCRs induced by the pulse lengths, the positive slopes of m values were 8.6/NLCR and 4.6/NLCR at the low- and high concentration in Fig. 6(a), respectively. On the other hand, a positive slope of 3.0/NLCR was found for the m gradient at the low concentration, whereas little changes were observed at the high concentration in Fig. 6(b). With the increase in NLCRs caused by acoustic pressures, irregular changes in m values and gradients were noticed at the low- and high concentrations in Figs. 6(c) and 6(d). With the increase in NLCRs due to frequency, the positive m slopes were 0.75/NLCR and 1.0/NLCR at the low- and high concentrations in Fig. 6(e), respectively. Slopes of m gradients were 0.2/NLCR and −0.04/NLCR at the low- and high concentrations in Fig. 6(f), respectively.

Figure 7 shows the impact of *in vitro* EMBs' nonlinearity controlled by the pulse length, negative peak pressure, and frequency on mean values and gradients of m parameters. With the increase in second harmonic NLCRs induced by the pulse lengths, the positive m slopes were 7.4/NLCR and 7.9/NLCR at the low- and high concentrations in Fig. 7(a), respectively. No noticeable changes in m gradients were observed in Fig. 7(b), which is different from the simulation
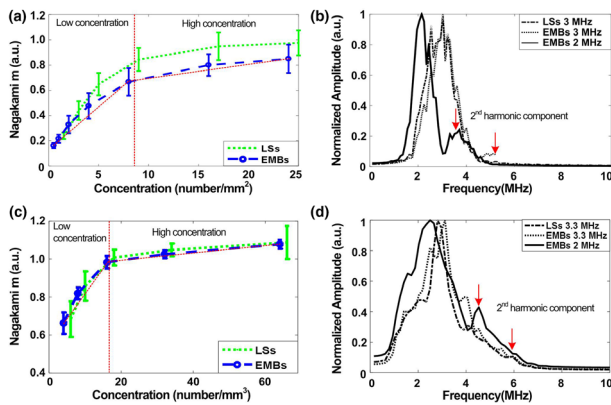
FIG. 4. The Nakagami *m* parameters of (a) simulated encapsulated microbubbles (EMBs) and linear scatterers (LSs) and (c) *in vitro* EMBs and LSs with increasing concentrations for the same acoustic parameters as in Fig. 1; the corresponding normalized power spectral density of (b) simulated EMBs and LSs and (d) *in vitro* EMBs and LSs. [Color figure can be viewed at wileyonlinelibrary.com]
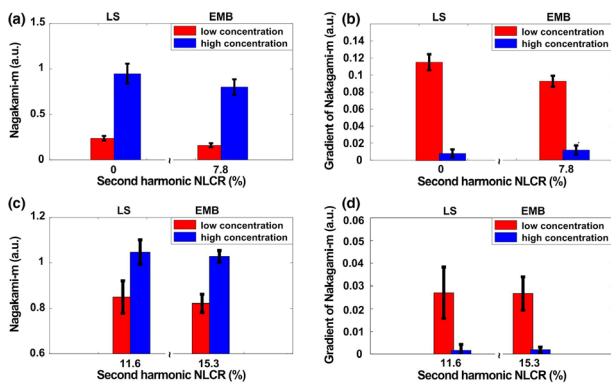

FIG. 5. Comparison of (a) the mean values and (b) gradients of Nakagami *m* parameters of encapsulated microbubbles (EMBs) and linear scatterers (LSs) for the low- and high-concentration segments under different second harmonic nonlinear-to-linear component ratios (NLCR) in simulations. The corresponding (c) mean values and (d) gradients of *m* parameters for *in vitro* experiments. The acoustic parameters are the same as in Fig. 1. [Color figure can be viewed at wileyonlinelibrary.com]

results. With the increase in NLCRs caused by the acoustic pressure, no positive and negative variations in *m* values and gradients were observed in Figs. 7(c) and 7(d). With the increase in NLCRs controlled by the frequency, the positive slopes of *m* values were 0.2/NLCR and 0.2/NLCR at the low- and high concentrations in Fig. 7(e), respectively. The positive slopes of gradients were 0.03/NLCR and 0.01/NLCR at the low- and high concentrations in Fig. 7(f), respectively.

4. DISCUSSION

4.A. Impact of NLCRs on Nakagami parameter for EMBs

The NLCRs of EMBs were altered by changing acoustic parameters of excitation pulses and corresponding changes in *m* values and gradients were analyzed to illustrate the impact

of EMBs' nonlinearity on Nakagami distributions. Compared with the corresponding changes in *m* gradients in Figs. 6 and 7, the alterations of *m* values of EMBs induced by the increase in NLCRs were more regular. Variations in *m* values and gradients with the increase in NLCRs induced by an increase in pulse length and a decrease in frequency were more obvious than corresponding alterations induced by an increase in acoustic pressure. Herein, the frequency coincided with the EMB resonant frequency when it was decreased[44,45]; in consequence, the second harmonic NLCRs were obviously enhanced and had the largest ranges of increase. The increase in NLCRs controlled by the frequency resulted in quasi-linear increases of *m* values in both simulations and experimental validations. These quasi-linearly increasing trends of *m* values might cause a slight shift right of the Nakagami distribution from Rayleigh–Gamma to pre-Rayleigh scattering. The corresponding shift was also observed in Fig. 3. These simulated and *in vitro* validations illustrate that the EMBs' nonlinearity distinctly influenced the Nakagami shape parameter and gradients. In other words, the Nakagami distribution of EMBs was affected by selected acoustic parameters. Therefore, the Nakagami distribution of EMBs is dependent on the system parameters, which are different from the lack of impact in the case of LSs in Ref. [3,46].

4.B. Comparison with other m parameter estimators

As presented in Fig. 4(a), *m* parameters characterized the relative concentration of EMBs within a sample size (resolution cell), which was related to the sample number and window size. The sample size might influence the estimation accuracy and stability of *m* parameters due to the heterogeneous distribution and boundary effect of local scatterers, which has been indicated in tissue characterization[1,11,12] but was unclear for nonlinear scattering produced by EMBs. Therefore, this dependency is illustrated here by comparing the estimation accuracy of five estimators under different sample numbers and window sizes, which was quantified by the RMSE between estimated *m* values and simulated ground truths in Fig. 8. For the same window size, RMSEs of all estimators for a high sample number in Fig. 8(b) were smaller than those at a small sample number in Fig. 8(a). For constant same sample numbers, RMSEs of all estimators were gradually reduced with increasing window sizes in Figs. 8(c) and 8(d). Among the five estimators, the GD estimator had the smallest RMSEs for the wide range of *m* values corresponding to pre- to post-Rayleigh distributions. Besides, the GD estimator had a relatively short operation time in Table II. Therefore, the GD estimator was used in this study.

Moreover, considering the estimation stability of the *m* parameter in tissue echoes, the window size was selected at least three times the ultrasound wavelength in previous studies.[3,10,19,23] However, the *m* estimation stability was limited when a fixed window size was used in some cases, which have been indicated in Ref. [[1,47]]. Thus, Tsui et al. proposed
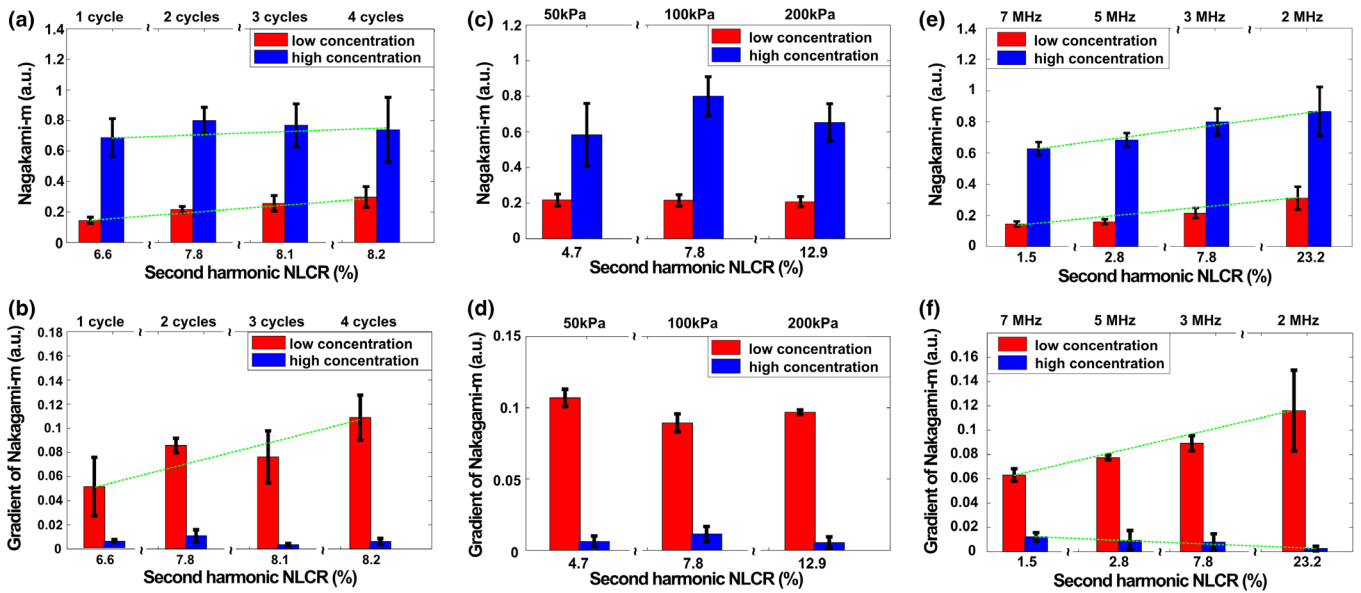
FIG. 6. In simulations, comparison of (a) mean values and (b) gradients of Nakagami *m* parameters for encapsulated microbubbles (EMBs) with increasing second harmonic nonlinear-to-linear component ratio (NLCR) attributed to an increase in pulse length from one to four cycles; the corresponding (c) mean values and (d) gradients for an increase in negative peak pressure from 50 to 200 kPa; and the corresponding (e) mean values and (f) gradients due to a decrease in frequency ranging from 7 to 2 MHz. [Color figure can be viewed at wileyonlinelibrary.com]
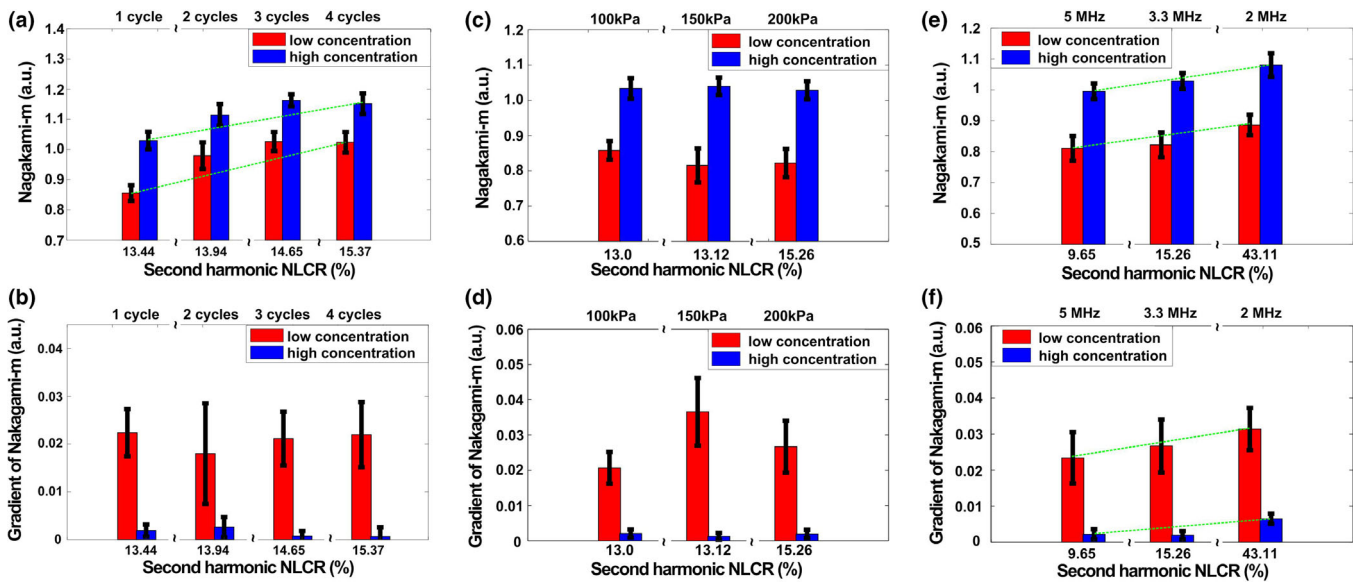

FIG. 7. *In vitro* experiments, comparison of (a) mean values and (b) gradients of Nakagami *m* parameters of encapsulated microbubbles (EMBs) with increasing second harmonic nonlinear-to-linear component ratio (NLCR) for an increase in pulse length from one to four cycles; the corresponding (c) mean values and (d) gradients for an increase in negative peak pressure from 100 to 200 kPa; and the corresponding (e) mean values and (f) gradients for a decrease in frequency from 5 to 2 MHz. [Color figure can be viewed at wileyonlinelibrary.com]

the window-modulated estimation method to balance the smoothness and discriminability of *m* estimations and then enhanced the stability for tissue characterization.[1] Compared with results using a fixed window size, the *m* estimation error using the window-modulated method at a modulation parameter of three was reduced to less than 5% and the mean *m* values were reduced after the averaging process.[1] Thus, the same modulation parameter was used in this study and

similar results were also observed. Compared with results obtained using a modulation parameter of 1, the standard deviation of simulated and *in vitro* *m* values was reduced $56.9 \pm 6.4\%$ ($P = 0.002$) but the corresponding *m* values were only decreased $4.9 \pm 5.6\%$ ($P = 0.09$) for the modulation parameter of 3. Therefore, the window-modulated compounding GD estimator was proposed to estimate *m* parameters of nonlinear EMBs in this study, which had
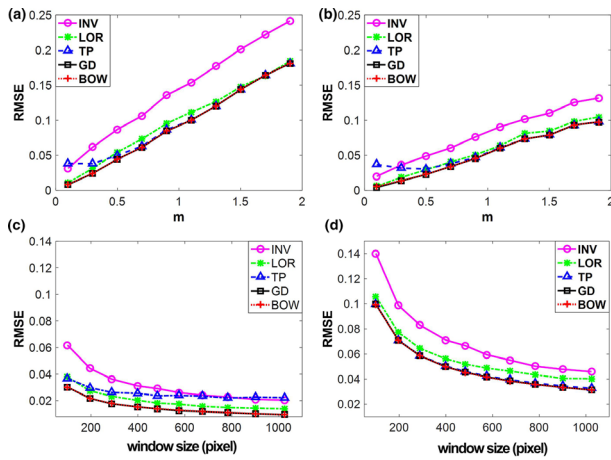
FIG. 8. Root-mean-square error (RMSE) between the simulated ground truths and the estimated values of Nakagami *m* parameters using various estimators. The RMSE of the increasing *m* parameters for sample numbers of (a) 200 and (b) 600; the RMSE of the fixed *m* parameters of (c) 0.5 and (d) 1.5 with increasing window size. The estimators include Greenwood–Durand, inverse normalized variance, Lorenz, Tolparev–Polyakov, and Bowman. [Color figure can be viewed at wileyonlinelibrary.com]

smaller RMSEs and standard deviations and better operational efficiency for a wide range of *m* values. In that case, the proposed estimator could avoid limitations of the sample size, could reduce disturbances from surrounding noise, heterogeneous distribution, and boundary effect of EMBs, and could then enhance the estimation accuracy and stability of the *m* parameter. The proposed estimator was beneficial to confirm that histograms fitted to Nakagami distributions in the case of EMBs and to illustrate that NLCRs of EMBs affected their Nakagami distributions, which supplemented previous results in Ref. [1,33].

4.C. Simulations vs *in vitro* experiments

Compared with changes induced by acoustic parameters in simulations, the pulse length, acoustic pressure, and frequency caused the same increase trends of NLCRs and almost similar changes in *m* values for *in vitro* experiments. However, when acoustic pressure was increased, no noticeable positive and negative changes were observed in the *m* values and gradients of EMBs both in simulations and *in vitro* experiments. With the increase in NLCRs induced by these pulse length and frequency, the change trends of *m* gradients were different in simulations and *in vitro* schemes at both the low- and high concentrations. As shown in Fig. 4, the *m* parameter was sensitive to the concentration of EMBs within a resolution cell. The variation in the concentration of EMBs would result in alterations of the B-mode envelope distribution and produce the change in *m* parameter. Thus,

the EMB concentration had to be precisely controlled in simulations and *in vitro* schemes to build the concentration–*m* relationship. In fact, compared with simulations, controlling and fixing the concentration and distribution of EMBs were very challenging for *in vitro* experiments.[30] Due to the time delay between dilution and detection during ultrasound examinations,[48] *in vitro* EMBs could exhibit natural rupture, dissolution, and disappearance[49,50] when the acoustic parameters were regulated for *in vitro* experiments. These inherent limitations in *in vitro* validations might cause a decrease in focal EMBs' concentration and an increase in regional shell fragments' concentration, which might result in a different change in *m* values, especially for gradients in *in vitro* experiments. Moreover, as shown in Figs. 4–7, there were larger standard deviations *in vitro* than those with simulations due to the above reasons.

4.D. Contributions and limitations

Since the *m* parameter had the capability of being sensitive to the relative concentration of tissue scatterers within a resolution cell,[3] a few studies had investigated the feasibility of EMBs' characterization using the Nakagami shape parameter.[28–31] However, as described in the introduction, information on Nakagami distribution of B-mode EMB images was scarce and the interaction between the nonlinearity of EMBs and the Nakagami model was also unknown in these previous reports. Therefore, although there were some inconsistent secondary results between simulations and *in vitro* experiments due to inherent limitations of experiments, these results not only verified the Nakagami distribution of EMBs but also illustrated the impact of EMBs' nonlinearity on the *m* parameter. Thus, the validation provided by this study not only illustrated the feasibility of EMBs' characterizations using the Nakagami model but also provided some necessary cross-verifications to enhance the reliability of EMBs' characterizations in future studies.

However, the simulation scheme was still limited by the vibration and scattering equation based on individual EMB, and by interactions between EMBs that were neglected in this study,[39] even if it overcame some limitations of *in vitro* experiments. Due to practical difficulties and complex factors, there are few multi-EMB vibration and scattering equations[39] and the current multicavitation-free bubble model without shell[51,52] is also inappropriate for characterization of EMBs with shell, but this was beyond the scope of this study. Additionally, the *in vitro* scheme was limited by selections of sample areas, disturbances by surrounding noise, and alterations of the regional concentration of EMBs induced by the needle size, injection rate,[53] flow

TABLE II. Operation time of different m estimators.

Estimator	INV	LOR	TP	GD	BOW
Operation time/s	21.4 ± 0.1	21.5 ± 0.04	51.7 ± 0.1	51.5 ± 0.1	103.2 ± 0.1

rate, and natural rupture and dissolution.[49,50] There would be also even more complex factors to consider under *in vivo* conditions. This would need to be addressed in future studies.

5. CONCLUSIONS

This study aimed to illustrate the impact of EMBs' nonlinearity regulated by acoustic parameters on the Nakagami distribution in order to analyze the feasibility of using statistical modeling of B-mode echoes for EMBs' characterization. The envelope distribution of simulated and *in vitro* images matched the corresponding Nakagami distribution with a high correlation coefficient. These results illustrated that Nakagami modeling has the potential to characterize nonlinear scatterers' distributions even if the Nakagami modeling is affected by the nonlinearity regulated by acoustic parameters. Therefore, this study provided numerical and *in vitro* validations to suggest potential applications of EMBs' characterization using Nakagami statistical model for diagnosis and therapy.

a)Authors to whom correspondence should be addressed. Electronic mails: chaoyingfu@qq.com; guy.cloutier@umontreal.ca; mxwan@mail.xjtu.edu.cn.

REFERENCES

1. Tsui PH, Ma HY, Zhou Z, Ho MC, Lee YH. Window-modulated compounding Nakagami imaging for ultrasound tissue characterization. *Ultrasonics*. 2014;54:1448–1459.
2. Renaud G, Bosch JG, van der Steen AFW, de Jong N. An, "acoustical camera" for in vitro characterization of contrast agent microbubble vibrations. *Appl Phys Lett*. 2012;100:101911.
3. Tsui PH, Chang CC. Imaging local scatterer concentrations by the Nakagami statistical model. *Ultrasound Med Biol*. 2007;33:608–619.
4. Bahbah N, Novell A, Bouakaz A, Djelouah H. Linear and nonlinear characterization of microbubbles and tissue using the Nakagami statistical model. *Ultrasonics*. 2017;76:200–207.
5. Wagner RF, Insana MF, Brown DG. Statistical properties of radio-frequency and envelope-detected signals with applications to medical ultrasound. *J Opt Soc Am A*. 1987;4:910–922.
6. Weng L, Reid JM, Shankar PM, Soetanto K. Ultrasound speckle analysis based on the K distribution. *J Acoust Soc Am*. 1991;89:2992–2995.
7. Dutt V, Greenleaf JF. Ultrasound echo envelope analysis using a homodyned K distribution signal model. *Ultrason Imaging*. 1994;16:265–287.
8. Shankar PM. A model for ultrasonic scattering from tissues based on the K distribution. *Phy Med Bio*. 1995;40:1633–1649.
9. Burckhardt CB. Speckle in ultrasound B-mode scans. *IEEE Trans Ultrason Ferroelectr Freq Control*. 1978;25:1–6.
10. Tsui PH, Yeh CK, Chang CC. Microvascular flow estimation by contrast-assisted ultrasound B-scan and statistical parametric images. *IEEE Trans Inf Technol B*. 2009;13:360–369.
11. Yamaguchi T. The quantitative ultrasound diagnosis of liver fibrosis using statistical analysis of the echo envelope. In: *Quantitative Ultrasound in Soft Tissues*. Dordrecht: Springer; 2013:275–288.
12. Shankar PM. A general statistical model for ultrasonic backscattering from tissues. *IEEE Trans Ultrason Ferroelectr Freq Control*. 2000;47:727–736.
13. Abdi A, Kaveh M. Performance comparison of three different estimators for the Nakagami m parameter using Monte Carlo simulation. *IEEE Commun Lett*. 2000;4:119–121.
14. Destrempes F, Cloutier G. Review of envelope statistics models for quantitative ultrasound imaging and tissue characterization. In: *Quantitative Ultrasound in Soft Tissues*. Dordrecht: Springer; 2013:219–274.
15. Destrempes F, Cloutier G. A critical review and uniformized representation of statistical distributions modeling the ultrasound echo envelope. *Ultrasound Med Biol*. 2010;36:1037–1051.
16. Oelze ML, Mamou J. Review of quantitative ultrasound: envelope statistics and backscatter coefficient imaging and contributions to diagnostic ultrasound. *IEEE Trans Ultrason Ferroelectr Freq Control*. 2016;63:336–351.
17. Han M, Wang N, Guo S, Chang N, Lu S, Wan M. Nakagami-m parametric imaging for characterization of thermal coagulation and cavitation erosion induced by HIFU. *Ultrason Sonochem*. 2018;45:78–85.
18. Jan J, Jirik R, Kolar R. Estimator comparison of the Nakagami-m parameter and its application in echocardiography. *Radioengineering*. 2004;13:8–12.
19. Liao YY, Tsui PH, Li CH, et al. Classification of scattering media within benign and malignant breast tumors based on ultrasound texture-feature-based and Nakagami-parameter images. *Med Phys*. 2011;38:2198–2207.
20. Tsui PH, Liao YY, Chang CC, Kuo WH, Chang KJ, Yeh CK. Classification of benign and malignant breast tumors by 2-D analysis based on contour description and scatterer characterization. *IEEE Trans Med Imaging*. 2010;29:513–522.
21. Ho MC, Tsui PH, Lee YH, et al. Early detection of liver fibrosis in rats using 3-D ultrasound Nakagami imaging: a feasibility evaluation. *Ultrasound Med Biol*. 2014;40:2272–2284.
22. Hsieh JW, Lee C, Chen Y, Lee W, Chiang H. Stage classification in chronic kidney disease by ultrasound image. Paper presented at: Proceedings of the 29th International Conference on Image and Vision Computing; 2014:271–276.
23. Zhang S, Shang S, Han Y, et al. Ex vivo and in vivo monitoring and characterization of thermal lesions by high-intensity focused ultrasound and microwave ablation using ultrasonic Nakagami imaging. *IEEE Trans Med Imaging*. 2018;37:1701–1709.
24. Zhang S, Li C, Zhou F, Wan M, Wang S. Enhanced lesion-to-bubble ratio on ultrasonic Nakagami imaging for monitoring of high-intensity focused ultrasound. *J Ultras Med*. 2014;33:959–970.
25. Cloutier G, Daronat M, Savéry D, Garcia D, Durand LG, Foster FS. Non-Gaussian statistics and temporal variations of the ultrasound signal backscattered by blood at frequencies between 10 and 58 MHz. *J Acoust Soc Am*. 2004;116:566–577.
26. Simpson DH, Chin CT, Burns PN. Pulse inversion Doppler: a new method for detecting nonlinear echoes from microbubble contrast agents. *IEEE Trans Ultrason Ferroelectr Freq Control*. 1999;46:372–382.
27. Wang D, Zhong H, Zhai Y, Hu H, Jin B, Wan M. Influence of guided waves in tibia on non-linear scattering of contrast agents. *Ultrasound Med Biol*. 2016;42:561–573.
28. Gu X, Wei M, Zong Y, Jiang H, Wan M. Flow quantification with Nakagami parametric imaging for suppressing contrast microbubbles attenuation. *Ultrasound Med Biol*. 2013;39:660–669.
29. Tsui PH, Yeh CK, Chang CC. Microvascular flow estimation by microbubble-assisted Nakagami imaging. *Ultrasound Med Biol*. 2009;35:653–671.
30. Kolar R, Jirik R, Harabiš V.Nakagami model of scattering in ultrasound contrast media. Paper presented at: IEEE International Ultrasonics Symposium; 2012:1–4.
31. Hu H, Xu S, Wang D, et al.Ultrasonic concentration imaging of cavitation bubbles using Nakagami statistical model. Paper presented at: IEEE International Ultrasonics Symposium; 2016:1–4.
32. Greenwood JA, Durand D. Aids for fitting the gamma distribution by maximum likelihood. *Technometrics*. 1960;2:55–65.

33. Lin JJ, Cheng JY, Huang LF, Lin YH, Wan YL, Tsui PH. Detecting changes in ultrasound backscattered statistics by using Nakagami parameters: comparisons of moment-based and maximum likelihood estimators. *Ultrasonics*. 2017;77:133–143.

34. Julian C, Beaulieu NC. Maximum-likelihood based estimation of the Nakagami m parameter. *IEEE Commun Lett*. 2001;5:101–103.

35. Errico C, Pierre J, Pezet S, et al. Ultrafast ultrasound localization microscopy for deep super-resolution vascular imaging. *Nature*. 2015;527:499–502.

36. Wang D, Xiao M, Hu H, et al. DCEUS-based focal parametric perfusion imaging of microvessel with single-pixel resolution and high contrast. *Ultrasonics*. 2018;84:392–403.

37. Greis C. Quantitative evaluation of microvascular blood flow by contrast-enhanced ultrasound (CEUS). *Clin Hemorheol Micro*. 2011;49:137–149.

38. Wang D, Zong Y, Yang X, et al. Ultrasound contrast plane wave imaging based on bubble wavelet transform: in vitro and in vivo validations. *Ultrasound Med Biol*. 2016;42:1584–1597.

39. Wang D, Hu H, Zhang X, et al. Bubble-echo based deconvolution of contrast-enhanced ultrasound imaging: simulation and experimental validations. *Med Phys*. 2018;45:4904–4103.

40. Morgan KE, Allen JS, Dayton PA, Chomas JE, Klibaov AL, Ferrara KW. Experimental and theoretical evaluation of microbubble behavior: effect of transmitted phase and bubble size. *IEEE Trans Ultrason Ferroelectr Freq Control*. 2000;47:1494–1509.

41. Zhao X, Zhong H, Wan M, Shen L. Ultrasound contrast imaging based on a novel algorithm combined pulse inversion with wavelet transform. *Ultrasound Med Biol*. 2011;37:1292–1305.

42. Tolparev R, Polyakov V. Estimation of the Nakagami probability-distribution parameters in a detector employing false-alarm probability stabilization. *Telecommun Radio Eng*. 1988;43:113–115.

43. Durning B, Laval J, Rognin N, Cachard C. Ultrasound signals and images simulation of phantoms with contrast agent. Paper presented at: IEEE International Ultrasonics Symposium; 2004:1–4.

44. Wang D, Zhang X, Sang Y, et al. Influence of guided waves in bone on pulse inversion contrast-enhanced ultrasound. *Med Phys*. 2019;46:3475–3482.

45. Wang D, Zhang Y, Hu H, Liu R, Zhong H, Wan M. Influences of frequency-dispersive guided waves on contrast-enhanced ultrasound imaging. Paper presented at: IEEE International Ultrasonics Symposium; 2016:1–4.

46. Shankar P. The use of the compound probability density function in ultrasonic tissue characterization. *Phy Med Bio*. 2004;49:1007–1015.

47. Tsui PH, Chen CK, Kuo WH, et al. Small-window parametric imaging based on information entropy for ultrasound tissue characterization. *Sci Rep-Uk*. 2017;7:41004.

48. Hettiarachchi K, Talu E, Longo ML, Dayton PA, Lee AP. On-chip generation of microbubbles as a practical technology for manufacturing contrast agents for ultrasonic imaging. *Lab Chip*. 2007;7:463–468.

49. Bouakaz A, Versluis M, de Jong N. High-speed optical observations of contrast agent destruction. *Ultrasound Med Biol*. 2005;31:391–399.

50. Chen WS, Matula TJ, Crum LA. The disappearance of ultrasound contrast bubbles: observations of bubble dissolution and cavitation nucleation. *Ultrasound Med Biol*. 2002;28:793–803.

51. Bremond N, Arora M, Ohl C-D, Lohse D. Controlled multibubble surface cavitation. *Phys Rev Lett*. 2006;96:224501.

52. Lu S, Xu S, Liu R, Hu H, Wan M. High-contrast active cavitation imaging technique based on multiple bubble wavelet transform. *J Acoust Soc Am*. 2016;140:1000–1011.

53. Talu E, Powell RL, Longo ML, Dayton PA. Needle size and injection rate impact microbubble contrast agent population. *Ultrasound Med Biol*. 2008;34:1182–1185.